Ghost Tomography: supplementary material

ANDREW. M. KINGSTON[1,2,*], DANIELE PELLICCIA[3], ALEXANDER RACK[4], MARGIE
P. OLBINADO[4], YIN CHENG[4], GLENN R. MYERS[1,2], AND DAVID M. PAGANIN[5]

[1]*Dept. Applied Mathematics, Research School of Physics and Eng., The Australian National University, Canberra, ACT 2601, Australia.*
[2]*CTLab: National Laboratory for Micro-CT, Advanced Imaging Precinct, The Australian National University, Canberra, ACT 2601, Australia.*
[3]*Instruments & Data Tools Pty Ltd, Victoria 3178, Australia.*
[4]*ESRF – The European Synchrotron, CS40220, F-38043 Grenoble, France.*
[5]*School of Physics and Astronomy, Monash University, Victoria 3800, Australia.*
[*]*Corresponding author: andrew.kingston@anu.edu.au*

This document provides supplementary information to "Ghost Tomography," https://doi.org/10.1364/optica.5.001516. The primary article contains the main results and analysis; however, in order for the findings to be reproducible, many more details must be conveyed on the methods. Here, we first present further experiment details. This is followed by a comprehensive description of the extensive data pre-processing performed. The techniques used for ghost imaging, i.e., recovering the transmission/projected-attenuation images, are then presented; first some benchmark results are established, then results from cross-correlation (XC), iterative XC (IXC), and regularized IXC are presented. Finally, two methods for ghost tomography are implemented, namely two-step and direct tomography; again a bench-mark result is provided for performance evaluation.

1. EXPERIMENT DETAILS

The experiment set-up is outlined in the primary article. Speckle images were created by illuminating a Nickel (Ni) foam with 26keV hard x-rays. This gave a good range of contrast with a mean transmission of 0.49 and a standard deviation of 0.243. Based on the dose-fractionation tomography simulations performed in Kingston et al. [1], we decided to use approximately 2000 speckle images per angular position. This was achieved by translating the foam over a 2D mesh of positions with 45 transverse steps of 0.4mm in both the vertical and horizontal directions. This gave a total of 2025 images per viewing angle.

The indirect detectors consisting of a LuAG:Ce (Ce-doped $Lu_3Al_5O_{12}$) single-crystal scintillator, $1\times$ lens and 2560×2160 pixel sCMOS camera used for measurement have a pixel pitch of 6.5μm. The sCMOS recording the primary beam used 0.1s exposure while the sCMOS recording the beam reflected by the beam-splitter used 0.5s exposure. The speckle images had $8.696\times$ greater intensity than the bucket images, indicating that the silicon beam-splitter had a diffraction efficiency of 2.25% for the given incident x-ray spectrum. Each image was cropped to include only illuminated regions. The speckle images were cropped to 1500×600 pixels. Due to spatial distortions in-

troduced by the beam-splitter crystal, the bucket image was cropped to 1448×751 pixels. Example speckle and bucket images are presented in Fig. 2 of the primary article.

Several beam losses forced the experiment to stop/restart several times. Foreseeing this problem, we knew that we would be unsure how many viewing-angles of data we may be able to collect. Therefore we used the quasi-random additive recurrence sequence to order viewing angles, as described in the primary article. Collating measurements from the various experiment restarts into complete *sets* of 2025 speckle/bucket image pairs resulted in 15 view-angles with a complete set of 2025 measurements at steps of 68.75° (modulo 360°), i.e., 30,375 measurements in total. Further analysis revealed that the x-ray beam was off for about 4000 consecutive measurements with the entire set of measurements for the eighth angle set (121.25°) missing and the seventh and ninth sets (52.5° and 10° respectively) only had about half of the 2025 speckle images each.

2. DATA PRE-PROCESSING

A significant amount of pre-processing was performed prior to attempting ghost-imaging and ghost-tomography. Much of this could not have been done had an actual single-pixel bucket detec-

tor been used. However, if care is taken in pre-characterizing the effects described below, it will be feasible to use a bucket detector in practice. In the following we describe the pre-processing steps we applied to the speckle/bucket image pairs; measured bucket values are estimated as the sum over all pixels in the bucket image. A multiplicative scale factor of 0.10984 is also applied to all speckle images to match the *flat-field* regions of the corresponding bucket images.

A. Motion blur

The point-spread function (PSF) of our x-ray ghost-imaging system was calculated as the normalized auto-covariance of the ensemble of illuminating spatially random fields (Fig. 2C) [2, 3]. This PSF has a full-width at half-maximum (FWHM) of 98μm. Observe however, the significant horizontal blurring of the bucket images with respect to the speckle images due to the motion of the Ni foam during data acquisition; the movement of the Ni foam to the next position was triggered by the primary beam sCMOS which had 0.1s exposure cf. 0.5s exposure for the bucket beam sCMOS. It was predicted that the magnitude of motion artifacts would be acceptable since it was approximately that of the expected final ghost-imaging resolution. Comparison of the Fourier power spectral density of the first speckle/bucket image pair (after applying a Hanning window) was used to find a blurring kernel that simulated the motion blur. The result (as presented in Fig. S1) is a Gaussian blurring kernel with standard deviation $\sigma(x, y) = (71.5, 19.5)\mu$m. Post blur the FWHM of the PSF increases to 139μm vertically and 240μm horizontally.
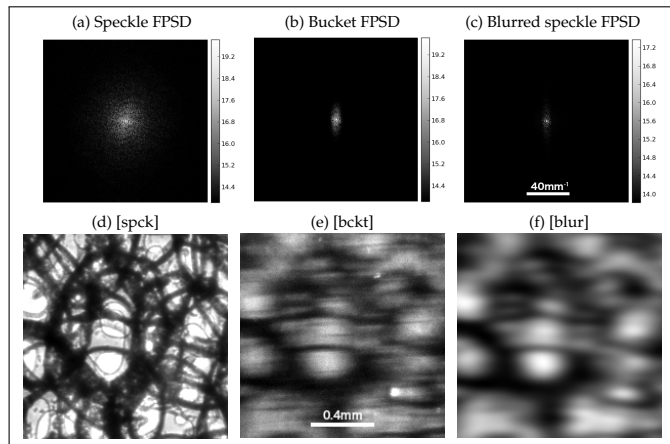

Fig. S1. (a) Image of the Fourier power spectral density (FPSD, logarithm of the magnitude of the Fourier transform) for the example speckle image. (b) 2D FPSD of corresponding bucket image. (c) 2D FPSD of speckle image after blurring with Gaussian kernel $\sigma(x, y) = (71.5, 19.5)\mu$m; This now matches the FPSD of (b). 200^2px (or 1.3×1.3 mm^2) example image subsets of (d) speckle, (e) corresponding bucket, and (f) speckle blurred by Gaussian kernel with $\sigma(x, y) = (71.5, 19.5)\mu m$ (matching motion artifacts in (e)).

Fourier ring correlation (FRC) [4, 5] can provide an estimate of resolution by comparing the correlation of two independent measurements of the same object at various spatial frequencies, (i.e., ring radii in Fourier space). Low correlation indicates a signal dominated by noise, and indicates the limit to measurement resolution. Here we compared a 200^2 pixel (or 1.3×1.3mm^2) image subset in the *flat-field* region beside the phantom (see Fig. S1d-f), from the first speckle field at $\theta = 0°$ and $\theta = 68.750°$.

The speckle images have full spatial resolution of 13μm (given a pixel dimension of 6.5μm). The bucket signal appears to have a reasonable resolution of approximately 25μm, however, we believe this is false resolution due to the correlation of crystal defects in the bucket images that are not affected by motion (e.g., the bright feature in the lower-right quadrant of Fig. S1e). Correlating the speckle image with the bucket image confirms this, indicating that the bucket image resolution is approximately 100μm and this corresponds well with the FRC analysis of the blurred speckle image with a raw speckle image. See Fig. 2E of primary article for FRC results.

B. Dark frames

The x-ray beam current was recorded in the header of the recorded speckle images. Speckle *dark-field* images (when the current was zero) were observed to have a mean intensity per pixel of approximately 100 counts while a speckle *flat-field* had a mean intensity per pixel of approximately 18,000 counts. All dark speckle/bucket image pairs were removed from the experimental data. An average of these pairs was used to estimate *dark-field* images that were subtracted from all remaining images.

C. Registration

An approximate global alignment between the speckle and bucket images was found manually on the first speckle/bucket pair by matching the speckle *flat-field* part of the bucket images (i.e., beside the sample). An offset of $(x, y) = (455, 156)\mu$m and a scale of $(x, y) = (1.0382, 1.0256)$ was estimated. Resulting image pairs (including the simulated motion blurring of the speckle) are shown in Fig. S2. A per-image-pair refinement of this registration was then performed by maximizing phase-correlation as described in Myers et al. [6]. The final dimensions of the registered full scale images became 1120×576 pixels.
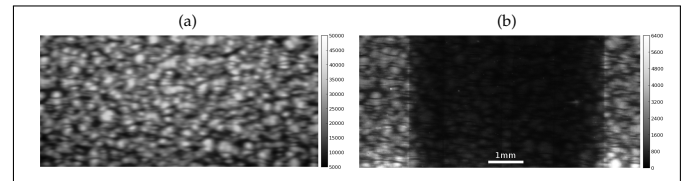

Fig. S2. (a) Example speckle image flipped vertically, magnified, translated, cropped, and blurred to match the speckle appearing in (b) the corresponding bucket image.

D. Intensity normalization

The recorded synchrotron x-ray beam current exhibited a *sawtooth* trend throughout the experiment with a variation of about 15% of the mean current. The variation is related to loss of electrons in the storage ring with time which is compensated by so-called refills appearing in equi-distant temporal intervals. The intensity of the speckle/bucket image pairs were normalized according to this beam current. Average speckle and bucket images were then computed at each angle (see e.g., Fig. S3a and S3b). A bright region may be observed at the top of the bucket image that corresponds to a dark region in the speckle image; the diffraction efficiency of the beam-splitter was higher in this region. Assuming a constant vertical profile of the flat-field regions over all average images, a scale was estimated for each image row to yield constant total counts per row. These average scale corrections were applied to all speckle and bucket images (see e.g., Fig. S3c and S3d).

E. Ring removal

Ring artifacts were evident due to non-idealities associated with the detector pixels, the associated x-ray scintillator, and the crystal beam-splitter. Affected pixels were identified using overall-average images, which should be smooth *a priori*, hence a median filtered image (using, in this case, a 5×17 pixel kernel) provided an estimate of the ideal average image. A per-pixel scale correction was identified from this and each measured image corrected accordingly. See Fig. S3e and S3f for an example of the resulting image; cf. Fig. S3c and S3d.
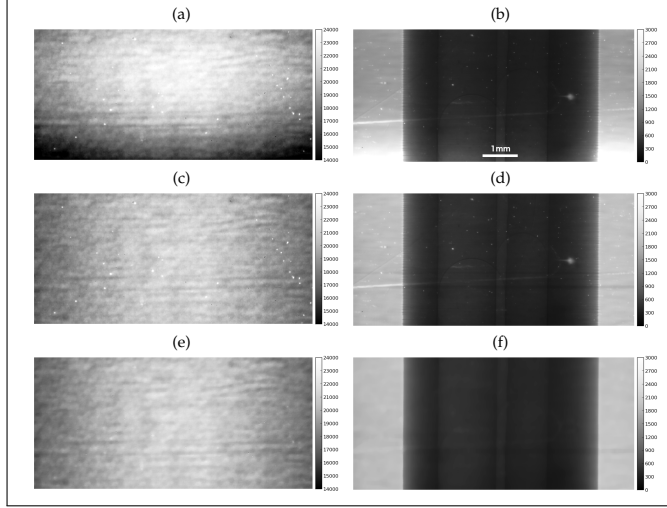

Fig. S3. Average images at $\theta = 0°$ of the a,c,e) speckle and b,d,f) bucket; a,b) as measured, c,d) after vertical flux variation was corrected, and e,f) after potential origins of ring artifacts were suppressed.

F. Identify rotation-axis

We determined average projected attenuation images at each angle as $-\log(\mathcal{B}/\mathcal{S})$, where $\mathcal{B}$ is the average bucket image and $\mathcal{S}$ is the average speckle image. The horizontal position of the projected rotation axis was found by performing tomographic reconstruction by filtered back-projection (FBP) of these attenuation images with a range of horizontal shifts, h. An example reconstruction where $h = 0\mu$m is given in Fig. S4a. As described in Kingston et al. [7], the resulting tomogram with the sharpest reconstructed volume yields the optimal value for h. This was found to be $h = 234\mu$m as depicted in Fig. S4b.

3. GHOST-IMAGING: RECOVERING TRANSMISSION IMAGES

A. Benchmark transmission images

The transmission, $\mathcal{B}/\mathcal{S}$, and projected attenuation images, $-\log(\mathcal{B}/\mathcal{S})$, can be estimated from the average of the speckle and bucket images at each angle. The images for $\theta = 0°$ are presented in Fig. S5. The transmission image in particular gives the objective function (or *benchmark*) for the performance of ghost image recovery in the following section; images of projected attenuation are required as the input for benchmark tomography in Sec. A.
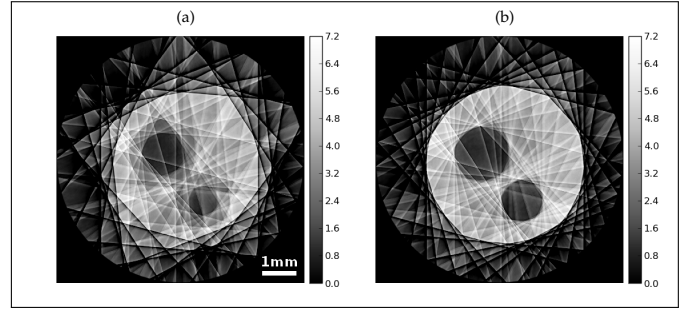

Fig. S4. Tomographic reconstruction by FBP of attenuation from the average images converted to projected attenuation, with various horizontal offsets of the rotation axis, h. a) The result with $h = 0\mu$m, i.e., axis in the center of the images. b) the optimal result with $h = 234\mu$m giving the sharpest tomogram.
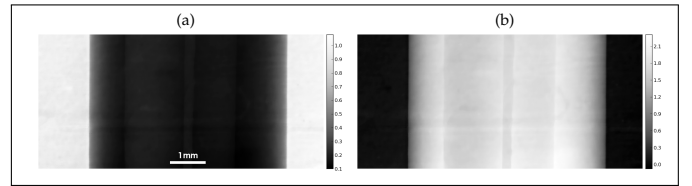

Fig. S5. a) The average transmission image at $\theta = 0°$. b) The corresponding linearized projected attenuation image.

B. Cross-correlation (XC) and iterative cross-correlation (IXC)

Transmission images, $T(x, y; \theta)$, at all $L = 14$ view-angles were recovered from the measured bucket values using (i) standard cross-correlation (XC) [8, 9], (ii) iterative XC (IXC), and (iii) IXC with smoothness priors. Methods (ii) and (iii) were executed as described in Kingston et al. [1]. Some example images with the data binned $16\times$ are presented in Fig. S6. In these cases, the iterative methods used 1120 iterations with Landweber regularization parameter $\gamma = 0.01/(J\sigma^2)$, where J is the number of measurements per view-angle and σ^2 is the average variance of the illumination images; the smoothness prior was executed as a Gaussian blur of the current estimate at each iteration with $\sigma(x, y) = (0.3, 0.45)$px. It can be observed from Fig. S6a-d that neither XC nor even IXC alone are sufficient; injecting priors in *maximum a-posteriori* methods, or *compressed sensing* is required to successfully extract the information present in the bucket measurements. In this case, asserting a smoothness prior significantly improved the ghost image as seen in Fig. S6e and S6f.

4. GHOST-TOMOGRAPHY

Two methods of performing ghost tomographic reconstruction were developed in Kingston et al. [1]: (1) standard tomography methods applied to recovered ghost projection-images, and (2) tomographic reconstruction directly from the bucket measurements. Here we have applied both methods for comparison. First, the objective (or *benchmark*) tomogram has been computed from the average projection-images generated in Sec. A.

A. Benchmark tomography

An iterative reconstruction technique is preferred given the limited number of viewing angles, $L = 14$, compared with 220 required to satisfy Nyquist angular sampling (when binned
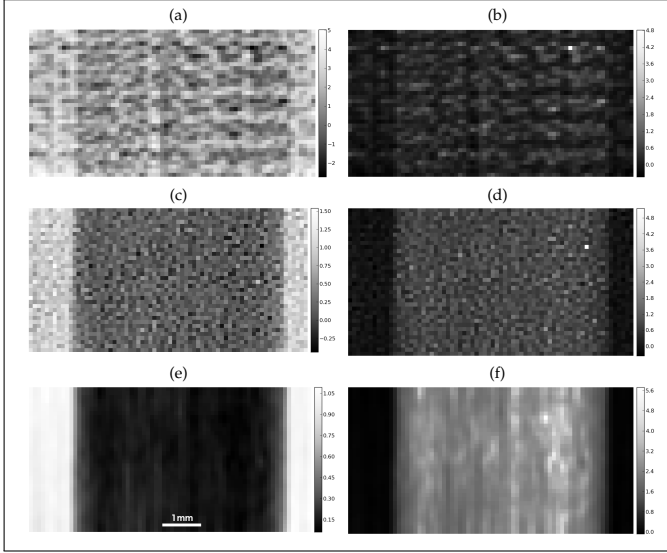
Fig. S6. a,c,e) Transmission images, and b,d,f) corresponding projected attenuation images, recovered from bucket measurements using a,b) cross-correlation (XC), c,d) 1120 iterations of iterative XC (IXC), and e,f) 1120 iterations of IXC with a smoothness prior.

×8). Here we have used gradient descent iterative reconstruction (GD-IR), or Landweber iteration, of the average linearized projected-attenuation images obtained in Sec. A, to give a *benchmark* tomogram for comparison with ghost tomography performance. The Landweber regularization parameter used here was $\gamma = 0.5/(NL)$ where N is the tomogram dimension in voxels. We have presented the results for various resolutions (binned ×8, ×16, and ×32), using $2N$ iterations of GD-IR in each case.
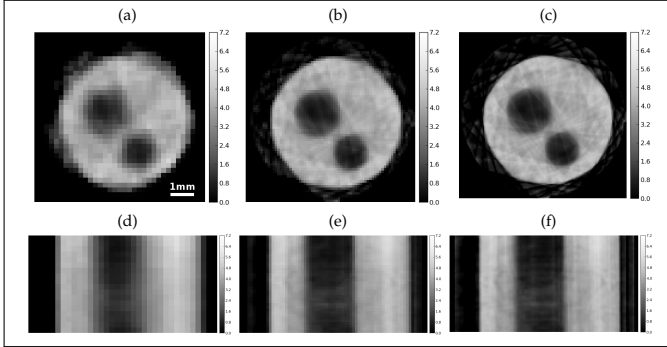

Fig. S7. a-c) central xy-slices, and d-f) yz-slices intersecting the large hole in the Al phantom, through tomograms resulting from GD-IR applied to average projected attenuation images. a,d) Binned ×32, using $2N = 70$ iterations. b,e) Binned ×16, using $2N = 140$ iterations. c,f) Binned ×8, using $2N = 280$ iterations. All reconstructions used a *zero* initial estimate with enforced positivity and a smoothness prior.

B. Two-step tomographic reconstruction: tomography from ghost-projections

As described in the primary article, applying conventional ghost-imaging, i.e., cross-correlation (XC), on a per view-angle basis, combined with standard tomography techniques (filtered back-

projection (FBP)) is insufficient to yield acceptable reconstructions (see Fig. S8a and S8d). Even using more sophisticated methods such as IXC per view-angle to recover projected-attenuation images followed by GD-IR to compute the tomogram produces a poor result (see Fig. S8b and S8e). Here $3N$ iterations were used with a Landweber regularization parameter of $\gamma = 0.2/(NL)$. Promising, but very noisy, results can be achieved using GD-IR applied to projection images recovered by IXC that incorporates a smoothness prior (see Fig. S8c and S8f). Here $2N$ iterations were used with a Landweber regularization parameter of $\gamma = 0.25/(NL)$.
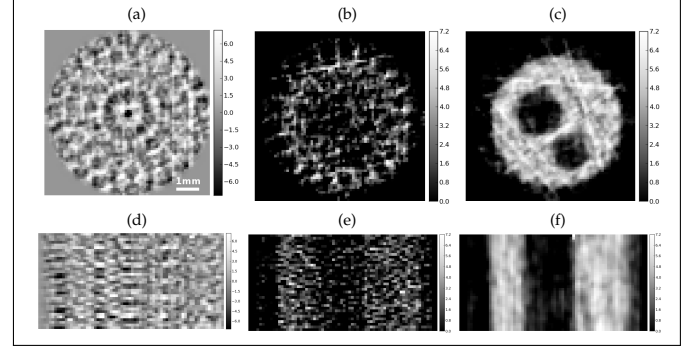

Fig. S8. Slices through tomography from ghost-images (binned 16×). a-c) Central xy-slices, and d-f) yz-slices intersecting the large hole in the Al phantom. Reconstruction by a,d) filtered back-projection (FBP) from XC projection images generated in Sec. B (e.g., see Fig. S6b). b,e) 210 iterations of GD-IR from the IXC projection images generated in Sec. B (e.g., see Fig. S6d). c,f) 140 iterations of GD-IR from projection images recovered through IXC with a smoothness prior as described in Sec. B (e.g., see Fig. S6f).

C. Direct tomographic reconstruction: tomography from bucket measurements

Here we consider direct tomographic reconstruction from bucket values, i.e., ghost tomography. The success of the two-step method described above (Sec. B) is limited since each ghost projection-image is recovered separately. Corrections made per iteration of IXC use only data per view-angle. An iterative reconstruction (IR) method that produces a volume directly from the bucket measurements uses the entire set of measured data per iteration; although slower, this can produce a superior result. In addition to this, priors applied in volume space are typically more powerful. For example, enforcing sparsity in gradient space by minimizing total-variation would be a useful prior in volume space that is not necessarily applicable in projection space.

Direct ghost tomography was developed in Sec. V of Kingston et al. [1] initially for both weakly absorbing objects as essentially 3D IXC; it was then generalized to the non-weakly absorbing case. Upon implementation, modifications were required to take the logarithm of the ghost projection-images since XC can commonly yield negative numbers. We replaced XC of $(B_j - \overline{B})$ with XC of $(B_j - \overline{B} + 0.05\breve{B})$ where $\overline{B}$ and $\breve{B}$ are the mean and standard deviation of bucket values, B_j for $j \in [0, J)$.

Again, gradient descent (or Landweber iteration) was used for IR. We used a Landweber regularization parameter of $\gamma = 0.5/(NL)$ with $32N$ iterations. A smoothness prior was incorporated as well as enforced positivity to improve the result.
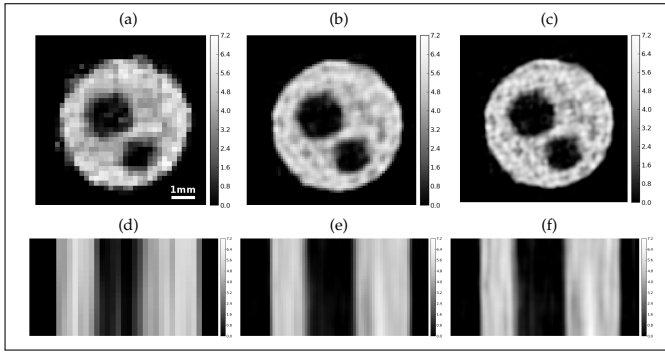
Fig. S9. a-c) Central xy-slices, and d-f) yz-slices intersecting the large hole in the Al phantom, through tomograms resulting from GD-IR with a smoothness prior in the volume applied directly to measured bucket values. a,d) Binned ×32, with *zero* initial estimate using 1120 iterations. b,e) Binned ×16, with upscaled result of a,c) as initial estimate using 2240 iterations. c,f) Binned ×8, with upscaled result of b,e) as initial estimate using 4480 iterations. All reconstructions enforced positivity and a smoothness prior.

Smoothness was reinforced per-iteration by blurring with a Gaussian kernel having $\sigma(x,y,z) = (0.25, 0.25, 0.5)$px. Typically, iterative tomographic reconstruction proceeds from an empty (or zero) initial volume. We observed in this case that gradient-descent x-ray ghost tomography became trapped in local minima when using such a starting point. This is most likely due to the highly under-constrained nature of the problem. Further research is required to determine if this is characteristic of iterative ghost-tomographic reconstruction. To overcome the problem we adopted a multi-scale approach where the initial seed for the IR at each scale was the prolongation of the IR output from the previous scale. At the coarsest scale (namely binning ×32 or 208μm voxel pitch), a zero initial estimate was used. The solution at each scale is presented in Fig. S9. Future work could involve a multi-grid solution, and consideration of more, or different, priors.

REFERENCES

1. A. M. Kingston, G. R. Myers, D. Pelliccia, I. D. Svalbe, and D. M. Paganin, "X-ray ghost tomography: denoising, dose fractionation and mask considerations," preprint at arXiv:1804.03370 (2018).
2. F. Ferri, D. Magatti, L. A. Lugiato, and A. Gatti, "Differential ghost imaging," Phys. Rev. Lett. **104** (2010). Article no. 253603.
3. D. Pelliccia, M. P. Olbinado, A. Rack, A. M. Kingston, G. R. Myers, and D. M. Paganin, "Towards a practical implementation of x-ray ghost imaging with synchrotron light," IUCrJ. **5**, 428–438 (2018).
4. W. Saxton and W. Baumeister, "The correlation averaging of a regularly arranged bacterial cell envelope protein," J. Microsc. **127**, 127–138 (1982).
5. M. Van Heel, W. Keegstra, W. Schutter, and E. Van Bruggen, "The structure and function of invertebrate respiratory proteins," in *Life Chemistry Reports Supplement 1,* E. Wood, ed. (1982), pp. 69–73.
6. G. R. Myers, A. M. Kingston, T. K. Varslot, and A. P. Sheppard, "Extending reference scan drift correction to high-magnification high-cone-angle tomography," Opt. Lett. **36**, 4809–4811 (2011).
7. A. Kingston, A. Sakellariou, T. Varslot, G. Myers, and A. Sheppard, "Reliable automatic alignment of tomographic projection data by passive auto-focus," Med. Phys. **38**, 4934–4945 (2011).
8. Y. Bromberg, O. Katz, and Y. Silberberg, "Ghost imaging with a single detector," Phys. Rev. A **79** (2009). Article no. 053840.
9. O. Katz, Y. Bromberg, and Y. Silberberg, "Compressive ghost imaging," Appl. Phys. Lett. **95** (2009). Article no. 131110.